

Lawrence Berkeley National Laboratory

LBL Publications

Title

Long-term simulation of space-charge effects

Permalink

<https://escholarship.org/uc/item/3tp8f4sn>

Author

Qiang, Ji

Publication Date

2019-02-01

DOI

10.1016/j.nima.2018.11.114

Peer reviewed

Long-term simulation of space-charge effects

Ji Qiang

Lawrence Berkeley National Laboratory, Berkeley, CA 94720

Abstract

The long-term macroparticle tracking simulation is computationally challenging but needed in order to study space-charge effects in high intensity circular accelerators. To address the challenge, in this paper, we proposed using a fully symplectic particle-in-cell model for the long-term space-charge simulation. We analyzed the artificial numerical emittance growth in the simulation and suggested using threshold numerical filtering in frequency domain to mitigate the emittance growth in the simulation. We also explored alternative frozen space-charge simulations and observed qualitative agreement with the self-consistent simulations.

1. Introduction

2 The nonlinear space-charge effects present strong limit on beam intensity in
3 high intensity/high brightness accelerators by causing beam emittance growth,
4 halo formation, and even particle loss. Self-consistent macroparticle simulations
5 have been widely used to study these space-charge effects in the accelerator
6 community [1, 2, 3, 4, 6, 5, 7, 8, 9, 10, 11, 12, 13, 14]. In some applications,
7 especially in high intensity circular accelerators such as a synchrotron, one has
8 to track the beam for many turns. It becomes computationally challenging for
9 the long-term space charge tracking simulation since on one hand, one needs
10 to avoid numerical artifacts and to ensure accuracy of the simulation results.

11 On the other hand, one would like to reduce the computing time in physics
12 applications.

13 The charged particle motion inside an accelerator follows classical Hamil-
14 tonian dynamics and satisfies the symplectic conditions. For better accuracy,
15 it is desirable to preserve the symplectic conditions in the long-term numerical
16 tracking simulation too. Violating the symplectic conditions in numerical inte-
17 gration results in unphysical results [15, 16]. A gridless symplectic space-charge
18 tracking model and a symplectic particle-in-cell (PIC) model were proposed in
19 recent studies [17, 18].

20 Even with the use of the symplectic space-charge model, there still exists ar-
21 tificial emittance growth in long-term space-charge simulations. This numerical
22 emittance growth could be due to numerical collisional effects associated with
23 the use of smaller number of macroparticles in the simulation compared with
24 the real number of particles inside the beam [19, 20, 21, 22, 23]. In this study,
25 we analyzed the numerical emittance growth in simulations using the symplec-
26 tic spectral PIC model and proposed a threshold filtering method to mitigate
27 the numerical emittance growth. In order to improve computational speed in
28 the long-term space-charge simulation, we also explored a frozen space-charge
29 model in the simulation.

30 The organization of this paper is as follows: after the introduction, we
31 present the symplectic particle-in-cell space-charge model in Section II; we ana-
32 lyzed the numerical emittance growth in self-consistent macroparticle tracking
33 and its mitigation in Section III; we tested the non-self consistent frozen space-
34 charge simulations in Section IV; and drew conclusions in Section V.

35 **2. Symplectic Particle-In-Cell Space-Charge Model**

36 In the self-consistent symplectic particle-in-cell (PIC) model, macroparticle
37 phase space coordinate advancing through a single step τ can be given as:

$$\begin{aligned}\zeta(\tau) &= \mathcal{M}(\tau)\zeta(0) \\ &= \mathcal{M}_1(\tau/2)\mathcal{M}_2(\tau)\mathcal{M}_1(\tau/2)\zeta(0) + O(\tau^3)\end{aligned}\quad (1)$$

38 where the transfer map \mathcal{M}_1 corresponds to the single particle Hamiltonian in-
39 cluding external fields and the transfer map \mathcal{M}_2 corresponds to the space-charge
40 potential from the multi-particle Coulomb interactions. The numerical integra-
41 tor Eq. 1 will be symplectic if both the transfer map \mathcal{M}_1 and the transfer map
42 \mathcal{M}_2 are symplectic. For a coasting beam inside a rectangular perfectly conduct-
43 ing pipe, the space-charge potential can be obtained from the solution of the
44 Poisson equation using a spectral method [18]. The one-step symplectic transfer
45 map \mathcal{M}_2 of particle i from the space-charge Hamiltonian is given as:

$$x_i(\tau) = x_i(0) \quad (2)$$

$$y_i(\tau) = y_i(0) \quad (3)$$

$$\begin{aligned}p_{xi}(\tau) &= p_{xi}(0) - \tau 4\pi K \sum_I \sum_J \frac{\partial S(x_I - x_i)}{\partial x_i} \times \\ &\quad S(y_J - y_i) \phi(x_I, y_J)\end{aligned}\quad (4)$$

$$\begin{aligned}p_{yi}(\tau) &= p_{yi}(0) - \tau 4\pi K \sum_I \sum_J S(x_I - x_i) \times \\ &\quad \frac{\partial S(y_J - y_i)}{\partial y_i} \phi(x_I, y_J)\end{aligned}\quad (5)$$

46 where both p_{xi} and p_{yi} are normalized by the reference particle momentum p_0 ,
47 $K = qI/(2\pi\epsilon_0 p_0 v_0^2 \gamma_0^2)$ is the generalized perveance, I is the beam current, ϵ_0 is
48 the permittivity of vacuum, p_0 is the momentum of the reference particle, v_0 is

49 the speed of the reference particle, γ_0 is the relativistic factor of the reference
50 particle, $S(x)$ is the unitless shape function (also called deposition function in
51 the PIC model), and ϕ denotes the interaction potential between grid point I
52 and J and is given as:

$$\phi(x_I, y_J) = \frac{4}{ab} \sum_{l=1}^{N_l} \sum_{m=1}^{N_m} \frac{1}{\gamma_{lm}^2} \sum_{I'} \sum_{J'} \bar{\rho}(x_{I'}, y_{J'}) \times \sin(\alpha_l x_{I'}) \sin(\beta_m y_{J'}) \sin(\alpha_l x_I) \sin(\beta_m y_J) \quad (6)$$

53 where a and b are the horizontal (x) and the vertical (y) aperture sizes re-
54 spectively, $\alpha_l = l\pi/a$, $\beta_m = m\pi/b$, $\gamma_{lm}^2 = \alpha_l^2 + \beta_m^2$, the integers I , J , I' , and
55 J' denote the two dimensional computational grid index, and the summations
56 with respect to those indices are limited to the range of a few local grid points
57 depending on the specific deposition function. The density related function
58 $\bar{\rho}(x_{I'}, y_{J'})$ on the grid can be obtained from:

$$\bar{\rho}(x_{I'}, y_{J'}) = \frac{1}{N_p} \sum_{j=1}^{N_p} S(x_{I'} - x_j) S(y_{J'} - y_j), \quad (7)$$

59 In the PIC literature, compact shape functions are used in the simulation.
60 For example, a quadratic shape function can be written as [24, 25]:

$$S(x_I - x_i) = \begin{cases} \frac{3}{4} - \left(\frac{x_i - x_I}{\Delta x}\right)^2, & |x_i - x_I| \leq \Delta x/2 \\ \frac{1}{2} \left(\frac{3}{2} - \frac{|x_i - x_I|}{\Delta x}\right)^2, & \Delta x/2 < |x_i - x_I| \\ & \leq 3/2\Delta x \\ 0 & \text{otherwise} \end{cases} \quad (8)$$

$$\frac{\partial S(x_I - x_i)}{\partial x_i} = \begin{cases} -2(\frac{x_i - x_I}{\Delta x})/\Delta x, & |x_i - x_I| \leq \Delta x/2 \\ (-\frac{3}{2} + \frac{(x_i - x_I)}{\Delta x})/\Delta x, & \Delta x/2 < |x_i - x_I| \leq 3/2\Delta x, \quad x_i > x_I \\ (\frac{3}{2} + \frac{(x_i - x_I)}{\Delta x})/\Delta x, & \Delta x/2 < |x_i - x_I| \leq 3/2\Delta x, \quad x_i \leq x_I \\ 0 & \text{otherwise} \end{cases} \quad (9)$$

62 where Δx is the mesh size in x dimension. The same shape function and its
 63 derivative can be applied to the y dimension. The explicit shape function and its
 64 derivative in the above equations results from the requirement of the symplectic
 65 condition [18].

66 Using the symplectic transfer map \mathcal{M}_1 for the single particle Hamiltonian
 67 including external fields from a magnetic optics code [26, 27, 28] and the transfer
 68 map \mathcal{M}_2 for space-charge Hamiltonian, one obtains a symplectic PIC model
 69 including the self-consistent space-charge effects.

70 3. Numerical Emittance Growth in Long-Term Simulation

71 In the long-term macroparticle space-charge tracking simulation, even with
 72 the use of self-consistent symplectic space-charge model, there still exists nu-
 73 merical emittance growth. To study this effect, we used a 1 GeV kinetic energy
 74 proton beam transporting inside a lattice that consists of 10 focusing-drift-
 75 defocusing-drift (FODO) lattice periods and one sextupole element per turn.
 76 The horizontal and the vertical aperture sizes are 6.5 millimeters. A schematic
 77 plot of the lattice is shown in Fig. 1. The zero current tune of the lattice is
 78 2.417. With 30 A beam current, the corresponding linear space-charge tune
 79 shift is 0.113. When the sextupole strength is set to zero, the lattice is a purely

80 linear FODO lattice. When the sextupole strength is nonzero, it can excite
 81 nonlinear resonance which will be further enhanced by the space-charge effects.



Figure 1: Schematic plot of a periodic FODO and sextupole lattice.

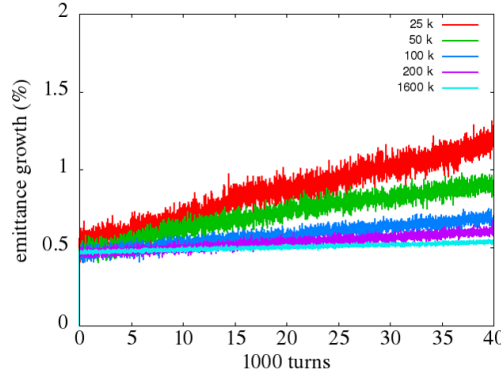


Figure 2: The 4D emittance growth evolution in a FODO lattice using 25, 50, 100, 200, and 1600 thousand macroparticles in the simulation.

82 Figure 2 shows the four dimensional (4D) emittance growth $(\frac{\epsilon_x}{\epsilon_{x0}} \frac{\epsilon_y}{\epsilon_{y0}} - 1)\%$
 83 evolution of the 1 GeV, 30A current proton beam through 40,000 turns of the
 84 above lattice with zero sextupole strength and using 25,000, 50,000, 100,000,
 85 200,000, and 1.6 million macroparticles and 64×64 spectral modes. The initial
 86 0.5% jump of emittance growth is due to charge redistribution to match into
 87 the lattice. It is seen that with the increase of the number of macroparticles,
 88 the emittance growth decreases. With the use of 1.6 million macroparticles,
 89 there is little emittance growth which is expected in this linear lattice. The
 90 extra emittance growth with smaller number of macroparticles is a numerical
 91 artifact.

92 The cause of this numerical artifact can be understood using a one-dimensional
 93 model. Following the spectral method used in the above symplectic PIC model
 94 for the space-charge potential, we calculated the sine function expansion mode

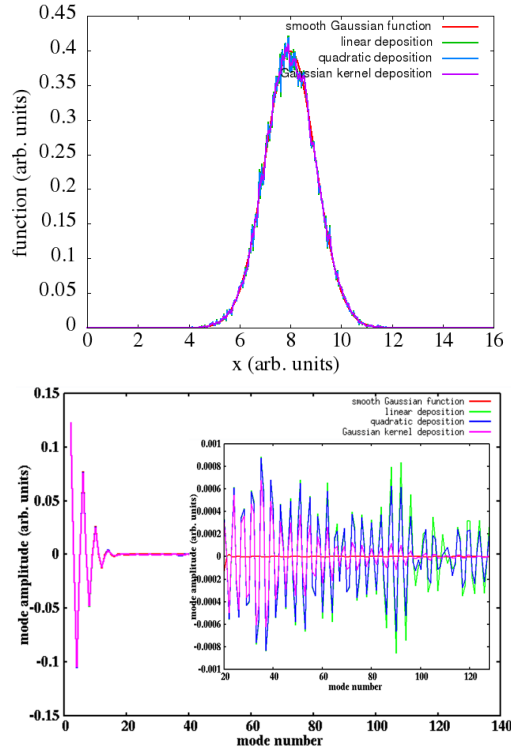


Figure 3: A Gaussian function (top), and its spectral mode amplitude (bottom) as a function of mode number from the smooth Gaussian function on the grid (red), from the linear particle deposition (green), the quadratic particle deposition (blue), and the Gaussian kernel particle deposition on the grid (magenta) using 25,000 macroparticles and 128 grid cells. The small plot inside the bottom figure is a zoom-in plot for mode number between 20 and 128.

95 amplitude from a smooth density distribution function on the grid and from a
 96 macroparticle sampled distribution function depositing onto the grid. Here, the
 97 amplitude of density mode l from the sampled macroparticle deposition is given
 98 as:

$$\rho^l = \frac{1}{N_p} \frac{2}{N_g \Delta x} \sum_i \sum_I S(x_I - x_i) \sin(\alpha_l x_i) \quad (10)$$

99 where N_p is the total number of macroparticles and N_g is the total number of
 100 grid cells. Figure 3 shows the mode amplitude as a function of mode number
 101 from the smooth Gaussian function on the grid, from the linear particle de-

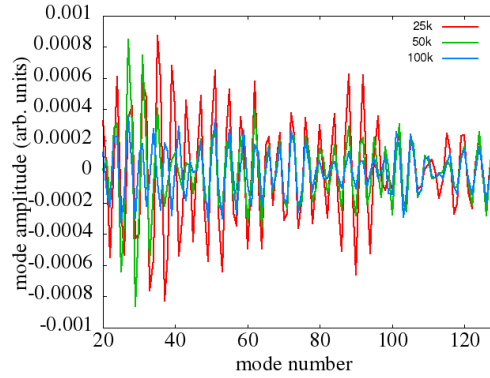


Figure 4: Mode amplitude of the Gaussian function as a function of mode number from the quadratic particle deposition using 25,000 (red), 50,000 (green) and 100,000 (blue) macroparticles and 128 grid cells.

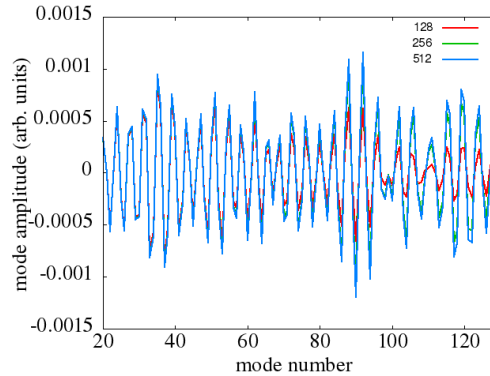


Figure 5: Mode amplitude of the Gaussian function as a function of mode number from the quadratic particle deposition using 25,000 and 128, 256 and 512 grid cells.

102 position, from the quadratic particle deposition, and from the Gaussian kernel
 103 particle deposition on the grid using 25,000 macroparticles and 128 grid cells.

104 Here, the Gaussian kernel particle deposition shape function is defined as:

$$S(x_I - x_i) = \begin{cases} \exp\left(-\frac{(x_i - x_I)^2}{2\sigma^2}\right); & |x_i - x_I| \leq 3.5\sigma \\ 0; & \text{otherwise} \end{cases} \quad (11)$$

105 and σ is chosen as the mesh size.

106 It is seen that for the smooth Gaussian distribution function, with mode

107 number beyond 20, the mode amplitude is nearly zero while the mode ampli-
 108 tude from the macroparticle deposition fluctuates with a magnitude of about
 109 10^{-4} . Those nonzero high frequency modes cause fluctuation in density dis-
 110 tribution and induce extra numerical emittance growth. The high frequency
 111 mode fluctuation amplitude becomes smaller from the linear deposition, to the
 112 quadratic deposition, and to the Gaussian kernel deposition. The difference
 113 between the linear deposition and the quadratic deposition is small. The Gaus-
 114 sian kernel deposition shows significantly smaller fluctuation for mode number
 115 greater than 60 since it corresponds to the infinite limit order of the polyno-
 116 mial deposition function [29]. The higher order deposition scheme spreads the
 117 macroparticle across multiple grid points and reduces the density fluctuation.
 118 However, the Gaussian kernel deposition is computationally more expensive in
 119 comparison to the other two deposition methods. It involves a number of expo-
 120 nential function evaluations (eight in this example) for each macroparticle and
 121 is a factor of about seven (or about five after some function optimization to re-
 122 duce the number of exponential function evaluation) slower than the quadratic
 123 deposition in this one dimensional example.

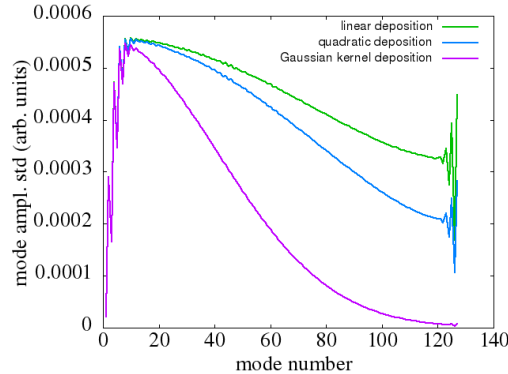


Figure 6: Mode amplitude standard deviation as a function of mode number from the linear particle deposition (green), the quadratic particle deposition (blue), and the Gaussian kernel particle deposition on the grid (magenta) using 25,000 macroparticles and 128 grid cells.

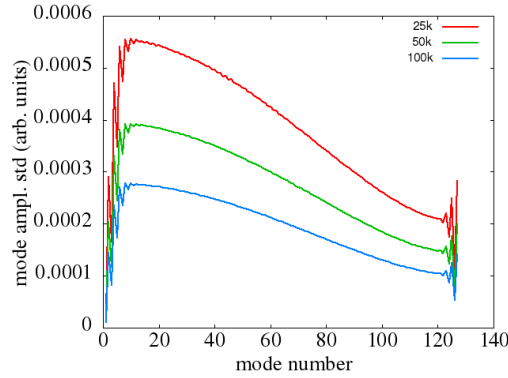


Figure 7: Mode amplitude standard deviation as a function of mode number from the quadratic particle deposition using 25,000 (red), 50,000 (green) and 100,000 (blue) macroparticles and 128 grid cells.

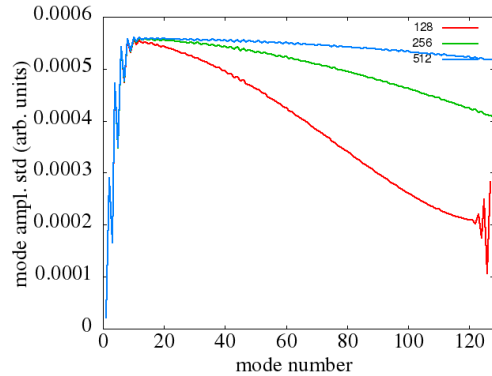


Figure 8: Mode amplitude standard deviation as a function of mode number from the quadratic particle deposition using 25,000 and 128, 256 and 512 grid cells.

124 The mode amplitude fluctuation from macroparticle deposition depends on
 125 the number of macroparticles used to sample the density distribution and the
 126 number of grid points. Figure 4 shows the mode amplitude of the Gaussian
 127 function as a function of mode number (≥ 20) from the quadratic deposition
 128 using 25,000, 50,000, and 100,000 macroparticles and 128 grid cells. With
 129 the increase of the number of macroparticles, the mode amplitude fluctuation
 130 becomes smaller. For a fixed macroparticle number, the mode amplitude fluctu-
 131 ation also depends on the number of grid cells used in the deposition. Figure 5

132 shows the mode amplitude of the Gaussian function as a function of mode num-
 133 ber (≥ 20) from the quadratic deposition using 128, 256, and 512 grid cells and
 134 25,000 macroparticles. As the number of grid cells increases, the mode am-
 135 plitude fluctuation becomes larger especially towards the larger mode number
 136 (≥ 70). The larger mesh size of less grid cell helps smooth out high frequency
 137 fluctuation.

138 The above fluctuation of the density mode amplitude from macroparticle
 139 deposition can be estimated quantitatively using the standard deviation (or
 140 variance) of the mode amplitude. Given the mode amplitude ρ^l in Eq. 10, the
 141 variance of ρ^l is given as:

$$var(\rho^l) = \frac{1}{N_p} var\left(\frac{2}{N_g \Delta x} \sum_I S(x_I - x_i) \sin(\alpha_l x_i)\right) \quad (12)$$

142 where

$$var\left(\frac{2}{N_g \Delta x} \sum_I S(x_I - x_i) \sin(\alpha_l x_i)\right) \approx \frac{1}{N_p} \left(\frac{2}{N_g \Delta x}\right)^2 \sum_i \left[\sum_I S(x_I - x_i) \sin(\alpha_l x_i)\right]^2 - \left(\frac{2}{N_g \Delta x}\right)^2$$

143 From the variance of each mode amplitude, one can calculate the standard
 144 deviation (std) of each mode amplitude by taking the square root of the variance.
 145 Figure 6 shows the mode amplitude standard deviation as a function of mode
 146 number for the above Gaussian function by using the linear deposition, the
 147 quadratic deposition, and the Gaussian kernel deposition. The mode amplitude
 148 standard deviation is small at small mode number and grows quickly to 10^{-4}
 149 level and start to decrease after about 10 modes. The standard deviation among
 150 the three deposition schemes becomes smaller as the order of deposition scheme
 151 becomes higher. The Gaussian kernel deposition shows least mode amplitude
 152 standard deviation which is consistent with the results in Fig. 3.

153 In Fig. 7, we show the mode amplitude standard deviation as a function of

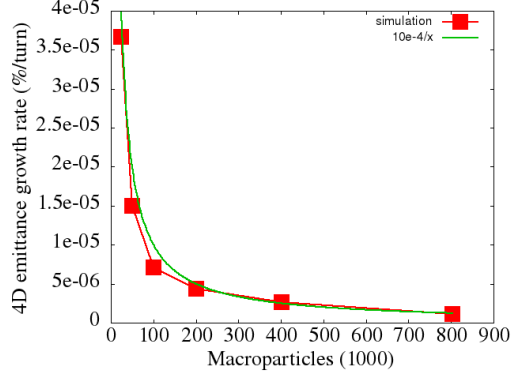


Figure 9: The 4D emittance growth rate as a function of the simulation macroparticle number using the FODO lattice.

154 mode number using 25,000, 50,000, and 100,000 macroparticle sampling of the
 155 Gaussian distribution. The standard deviation decreases with the increase of the
 156 macroparticle number and scales as $1/\sqrt{N_p}$ as expected from Eq. 12. Figure 8
 157 shows the mode amplitude standard deviation as a function of mode number
 158 using 128, 256, and 512 grid cells and 25,000 macroparticles for the above
 159 Gaussian distribution. For small mode number (less than 10), the standard
 160 deviation is close among three numbers of grid cells. For larger mode number,
 161 the standard deviation of the small number of grid cells is smaller, which is also
 162 seen in Fig. 5.

163 The error in the charge density mode amplitude results in error in the solu-
 164 tion of space-charge potential and the corresponding force in momentum update
 165 in Eqs. 4-5. Assume that the error of force in x momentum update is δF , after
 166 one step τ , i.e. $x_2 = x_1$, $x'_2 = x'_1 + \delta F\tau$, the new emittance under the effect of
 167 this force will be:

$$\begin{aligned}
 \epsilon_2^2 &= \langle x_2^2 \rangle \langle x_2'^2 \rangle - \langle x_2 x_2' \rangle^2 \\
 &= \langle x_1^2 \rangle \langle x_1'^2 \rangle - \langle x_1 x_1' \rangle^2 + \\
 &\quad 2(\langle x_1^2 \rangle \langle x_1' \delta F \rangle - \langle x_1 x_1' \rangle \langle x_1 \delta F \rangle) \tau + (\langle x_1^2 \rangle \langle \delta F^2 \rangle - \langle x_1 \delta F \rangle^2) \tau^2
 \end{aligned}$$

168 where $\langle \rangle$ denotes the average with respect to the particle distribution. The
 169 above equation can be rewritten as:

$$\epsilon_2^2 = \epsilon_1^2 + 2(\langle x_1^2 \rangle \langle x_1' \delta F \rangle - \langle x_1 x_1' \rangle \langle x_1 \delta F \rangle) \tau / \epsilon + (\langle x_1^2 \rangle \langle (\delta F)^2 \rangle - \langle x_1 \delta F \rangle^2) \tau^2 / \epsilon^2$$

170 and the emittance growth due to this error will be:

$$\Delta \epsilon \approx (\langle x^2 \rangle \langle x' \delta F \rangle - \langle x x' \rangle \langle x \delta F \rangle) \tau / \epsilon + \frac{1}{2} (\langle x^2 \rangle \langle (\delta F)^2 \rangle - \langle x \delta F \rangle^2) \tau^2 / \epsilon^2$$

171 If δF is a linear function of the position x , the emittance growth will be zero as
 172 expected since the linear force will not change the beam emittance. If δF is a
 173 random error force with zero mean and independent of x and x' , the emittance
 174 growth would be

$$\frac{\Delta \epsilon}{\tau} \approx \frac{1}{2} \langle x^2 \rangle \langle (\delta F)^2 \rangle \tau / \epsilon \quad (17)$$

175 which is in agreement with the result of reference [23]. Assume that this error
 176 is due to mode amplitude fluctuation of the finite number of macroparticles
 177 sampling, from the above example, we see that $\langle (\delta F)^2 \rangle \propto 1/N_p$. This suggests
 178 that the numerical emittance growth would decrease as more macroparticles are
 179 used. If δF is not a purely random error force (e.g. due to systematic truncation
 180 error), the dependence of the emittance growth on the number of macroparticle
 181 is more complicated. Figure 9 shows the 4D emittance growth rate as a function
 182 of macroparticle number in the linear FODO lattice using 256×256 grid cells.
 183 It is seen that the emittance growth rate scales as $1/N_p$, which agrees well with
 184 the scaling of the random sample fluctuation induced emittance growth.

185 In the above example, we used a linear FODO lattice with zero sextupole

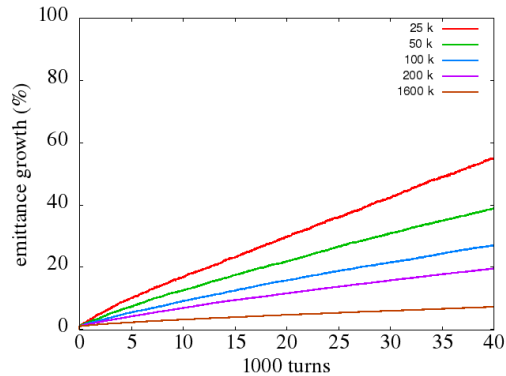


Figure 10: The 4D emittance growth evolution in the FODO and sextupole lattice using 25, 50, 100, 200, and 1600 thousand macroparticles in the simulation.

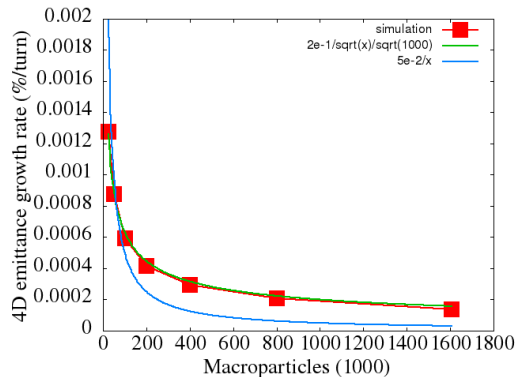


Figure 11: The 4D emittance growth rate as a function of macroparticle number using the FODO and sextupole lattice.

186 strength. When the sextupole strength is nonzero, it can excite third order
 187 resonance. Figure 10 shows the 4D emittance growth evolution of the 30 A
 188 proton beam inside a lattice with an effective $10/m/m$ integrated sextupole
 189 strength using several macroparticle numbers and 64×64 modes. Besides the
 190 physical emittance growth caused by the resonance, there also exists significant
 191 numerical emittance growth due to the finite macroparticle sampling. Figure 11
 192 shows the emittance growth rate in this case as function of the macroparticle
 193 number. It appears that in this case, the emittance growth rate scales close
 194 to $1/\sqrt{N_p}$. This slower scaling with respect to the N_p might be due to the

195 interaction between the numerical force error and the nonlinear resonance.

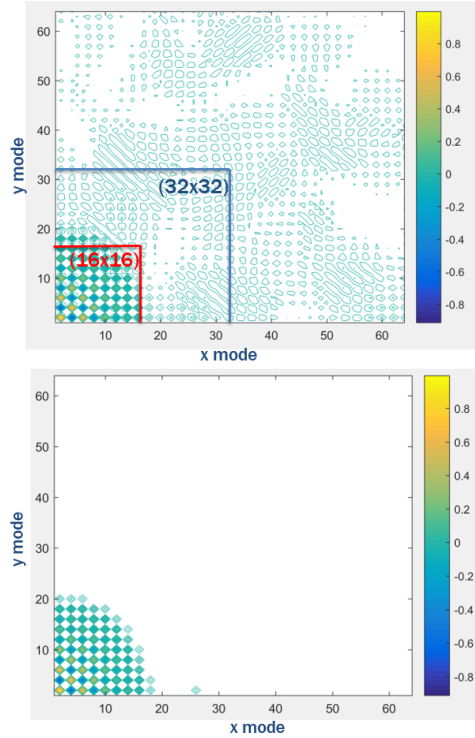


Figure 12: The mode amplitude of a 2D Gaussian distribution without (top) and with 1% threshold filter (bottom).

196 The charge density fluctuation from the macroparticle sampling can be fur-
197 ther smoothed out by using a numerical filter in frequency domain besides em-
198 ploying the shape function for particle deposition. As seen from the above one-
199 dimensional example, the shape function helps suppress high frequency errors.
200 However, even with the use of the shape function, there still exists significant
201 level of mode amplitude error fluctuation for mode number greater than 20.
202 Those mode amplitude errors can be removed by numerical filtering in the fre-
203 quency domain. Instead of using a standard cut-off method that removes all
204 modes beyond a given mode number (i.e. cut-off frequency), we proposed using
205 an amplitude threshold method to remove unwanted modes. The mode with

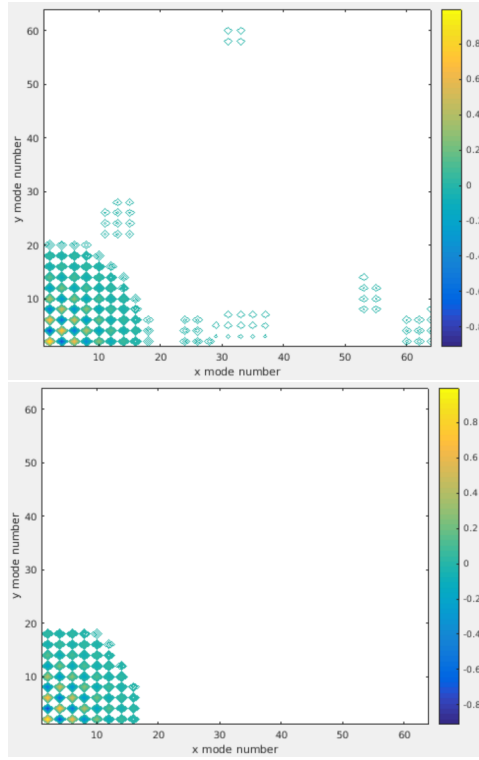


Figure 13: The mode amplitude of a 2D Gaussian distribution with two sigma standard deviation (top) and with four sigma standard deviation threshold filter (bottom).

206 an amplitude below the threshold value is removed from the density distribu-
 207 tion. The advantage of this method is instead of removing all high frequency
 208 modes, it will keep the high frequency modes with large amplitudes. These
 209 modes can represent real physics structures inside the beam. The threshold
 210 also removes the unphysical low frequency modes associated with the small
 211 number of macroparticle sampling. Here, we explored two threshold methods.
 212 In the first threshold method, the threshold value is calculated from a given
 213 fraction of the maximum amplitude of the density spectral distribution. In the
 214 second method, the threshold value is defined as a few standard deviations of
 215 the mode amplitude as shown in the one-dimensional Gaussian function exam-
 216 ple. The mode with an amplitude below the threshold value is regarded as

217 numerical sampling error due to the use of small number of macroparticles and
 218 is removed from the density distribution. The advantage of the first method
 219 is that the threshold value is readily attainable from the density spectral dis-
 220 tribution. The disadvantage of this method is that the threshold fraction is
 221 an external supplied hyperparameter. The advantage of the second method is
 222 that the threshold value is calculated dynamically through the simulation. The
 223 disadvantage of this method is the computational cost to obtain the standard
 224 deviation of each mode. The total computational cost of those standard de-
 225 viations is proportional to the number of modes multiplied by the number of
 226 macroparticles. This makes computing the mode amplitude standard deviations
 227 more expensive than computing the mode amplitudes (proportional to the num-
 228 ber of macroparticles) and not affordable at every time step. In practice, these
 229 mode amplitude standard deviations can be computed once (or once in while)
 230 during the simulation and reused in the following simulation. Figure 12 shows
 231 the spectral amplitude of a 2D Gaussian density distribution without and with
 232 0.01 threshold filter using 128×128 grid cells and 25,000 macroparticles with
 233 the quadratic deposition method. The standard cut-off filter with 16×16 and
 234 32×32 modes are also indicated in above plot. Most high frequency noise is
 235 removed in this distribution by using the threshold filtering method. Figure 13
 236 shows the above sampled spectral amplitude distribution by using the threshold
 237 values of two-sigma standard deviation and four-sigma standard deviation. The
 238 two-sigma standard deviation threshold value does not remove all the higher
 239 frequency errors.

240 As a test of the threshold filtering method, we reran the above space-charge
 241 long-term simulation in the linear FODO lattice using 0 (no filtering), 0.005,
 242 0.01 and 0.05 threshold filtering the charge density in the simulation and 25,000
 243 macroparticles and the brute force direct cut-off filtering. Here, the larger

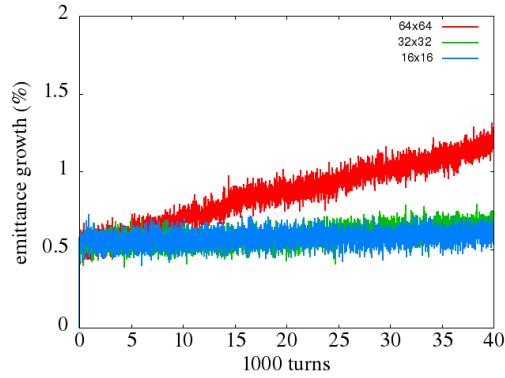


Figure 14: The 4D emittance growth with 64×64 , 32×32 , 16×16 modes cut-off filtering of the charge density distribution using 25k in the FODO lattice.

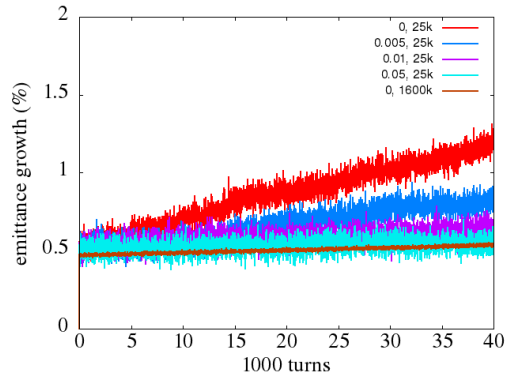


Figure 15: The 4D emittance growth with 0 (no filtering) with 0.005, 0.01 and 0.05 threshold filtering of charge density distribution using 25k macroparticles and 0 filtering using 1600k macroparticles in the FODO lattice.

244 threshold value, the less number of modes will be included in the simulation.
 245 Those results are shown in Figs. 14-15. It is seen that without numerical fil-
 246 tering, there is significant emittance growth after 40,000 turns. With 0.05
 247 threshold filtering, there is little emittance growth, which is consistent with the
 248 expected physics emittance growth by using 1600k macroparticles without fil-
 249 tering. Both the brute force filtering and the threshold filtering work well in
 250 this case.

251 We also reran the simulation of 30A proton beam transport in a lattice in-

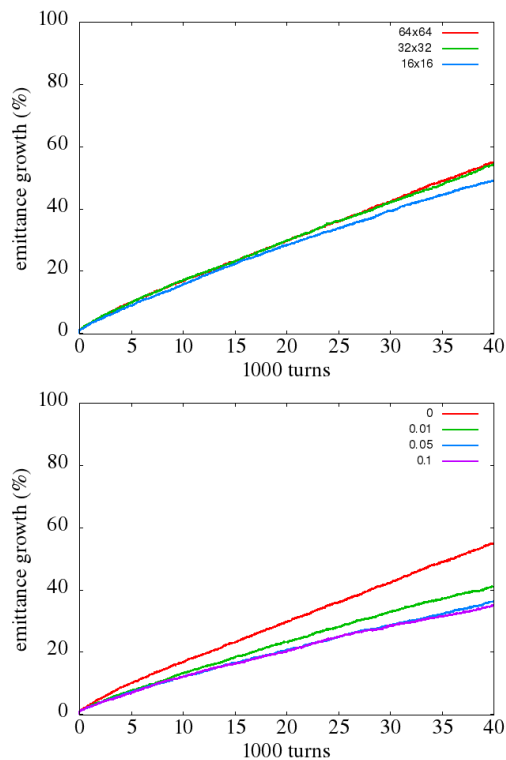


Figure 16: The 4D emittance growth using 64×64 , 32×32 , 16×16 modes (top) and with 0 (no filtering) with 0.01, 0.05 and 0.1 threshold filtering (bottom) of charge density distribution using 25k macroparticles in a FODO and sextupole lattice.

252 including nonlinear sextupole element shown in Fig. 10. The 4D emittance growth
 253 evolutions using the brute force cut-off and the threshold filtering are shown in
 254 Fig. 16. It is seen that even with 16×16 mode cut-off filtering, there still ex-
 255 ists significant emittance growth, while a threshold value 0.1 helps significantly
 256 lower the emittance growth. Using the four-sigma standard deviation threshold
 257 value yields similar emittance growth to the fraction threshold (0.1) as shown in
 258 Fig. 17. The amplitude threshold filtering works better than the cut-off filtering
 259 in this case because it removes not only the unwanted high frequency errors
 260 but also the unwanted low frequency errors, while the cut-off filtering removes
 261 only the high frequency errors. Those low frequency errors interact with the

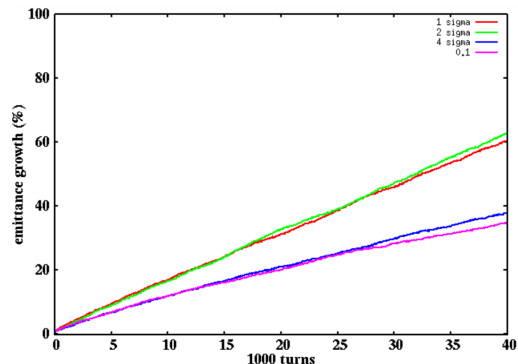


Figure 17: 4D emittance growth with one sigma, two sigma, four sigma standard deviation and 0.1 maximum amplitude threshold filtering of charge density distribution using 25k macroparticles in a FODO and sextupole lattice.

262 nonlinear resonance and cause extra emittance growth.

263 4. Frozen Space-Charge Simulation

264 In order to improve computational speed in the long-term simulation, we also
 265 explored a frozen space-charge model during the simulation [30, 31, 32]. Here,
 266 instead of self-consistently updating the space-charge calculation at every time
 267 step, after some initial time steps, we store the solutions of the space-charge
 268 potential along the lattice and reuse those stored space-charge potentials for
 269 the following long-term simulation. This model assumes that after some initial
 270 time steps, the charge density distribution will not vary significantly from turn
 271 to turn.

272 Figure 18 shows the total 4D emittance growth evolution inside the above
 273 linear FODO lattice example from the simulation using the self-consistent track-
 274 ing and from the simulation using the frozen space-charge model after initial 200
 275 turns with 0.05 threshold filtering, 128×128 grid cells, and 25,000 macropar-
 276 ticles. It is seen that emittance growth evolution from the frozen space-charge
 277 simulation agrees with that from the self-consistent simulation quite well. The
 278 computational speed of the frozen space-charge simulation is about a factor of

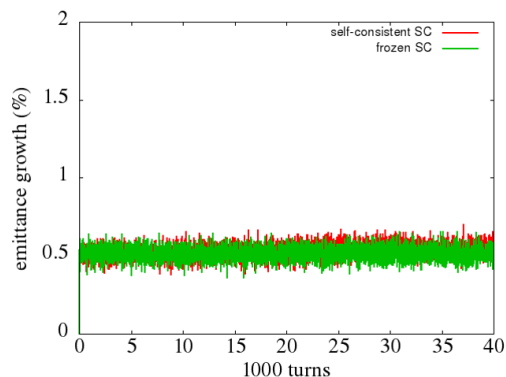


Figure 18: The 4D emittance growth evolution from the self-consistent simulation (red) and the frozen space-charge simulation (green) in a FODO lattice.

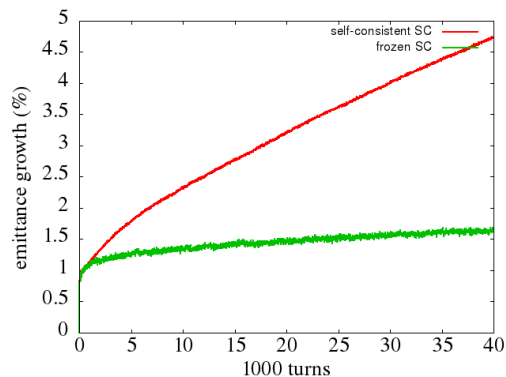


Figure 19: The 4D emittance growth evolution from the self-consistent simulation (red) and the frozen space-charge model (green) in a FODO and sextupole lattice.

279 six faster than the self-consistent simulation in this case.

280 We also ran the 30 A proton beam through the FODO and sextupole lat-
 281 tice using the frozen simulation and the self-consistent simulation. Figure 19
 282 shows the 4D emittance growth evolution from the frozen space-charge simula-
 283 tion together with the emittance growth from the self-consistent space-charge
 284 simulation with 1.6 million macroparticles and 0.1 threshold filtering. The emit-
 285 tance growth from the self-consistent simulation has converged with respect to
 286 the number of macroparticles. In this example, both the frozen space-charge
 287 simulation and the self-consistent simulation show emittance growth driven by

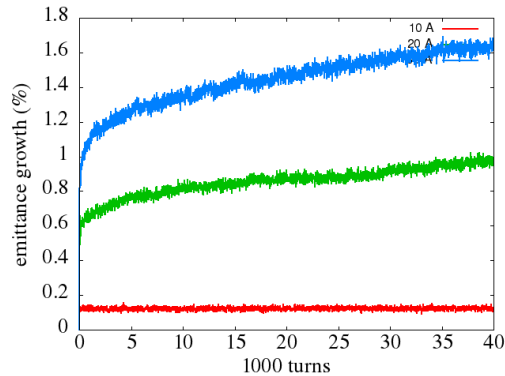


Figure 20: The 4D emittance growth evolution from the frozen space-charge model simulation with 10A, 20A and 30A beam currents in a FODO and sextupole lattice.

288 the third order resonance, while the frozen simulation shows significantly less
 289 emittance growth.

290 Figure 20 shows the 4D emittance growth evolution of the 1 GeV proton
 291 beam through the above FODO and sextupole lattice with 10A, 20A, and 30A
 292 beam current from the frozen space-charge simulation. It is seen that with small
 293 current, there is little emittance growth caused by the third-order resonance.
 294 This is due to the fact that the lattice tune working point is 2.417, and the lin-
 295 ear space-charge tune shift 0.038 with 10A, 0.075 with 20A, and 0.113 with 30A
 296 current. With the increase of the current from 10A to 30A, more and more par-
 297 ticles move into the 3rd order (2.333) resonance and results in larger emittance
 298 growth as observed in the simulation. The frozen space-charge simulation qual-
 299 itatively reproduce the physical results of resonance driven emittance growth,
 300 which was also observed in the self-consistent space-charge simulation [18].

301 5. Conclusion

302 The long-term macroparticle tracking simulation is computationally chal-
 303 lenging but needed for the study of space-charge effects in high intensity circular
 304 accelerators such as a synchrotron. In this study, we propose using symplectic

305 PIC model with the threshold filtering in frequency domain and frozen space-
306 charge model to address those challenges.

307 There exists slow numerical emittance growth in the long-term simulation
308 even with the use of symplectic space-charge model. This numerical emittance
309 could be caused by the high frequency density fluctuation or unphysical low fre-
310 quency density modes associated with the use of small number of macroparticles.
311 In a linear lattice without nonlinear resonance, the artificial emittance growth
312 rate scales inversely as the number of macroparticles when the random sam-
313 pling error is dominant. In a nonlinear lattice, the artificial emittance growth
314 rate scaling becomes more complicated due to the interaction between the low
315 frequency error and the nonlinear resonance.

316 The numerical artifacts from macroparticle sampling can be mitigated by
317 the use of threshold filtering in frequency domain. By appropriately choosing
318 threshold value, the numerical emittance growth can be significantly reduced
319 in the long-term simulation. Here, we proposed two types of threshold values.
320 One type of threshold value is a predefined fraction of the maximum amplitude
321 of the charge density spectral distribution. The other type of threshold value
322 is based on the standard deviation of mode amplitude and can be dynamically
323 calculated from the particle distribution in the simulation (this can be compu-
324 tationally expensive). Both types of threshold values yield similar simulation
325 results with appropriate choice of threshold values. The use of numerical filter-
326 ing is under the situation where significant numerical emittance growth observed
327 in the simulation.

328 In order to improve the computing speed, we also explored a frozen space-
329 charge model that stores the space-charge potential solutions after some initial
330 time steps and reuse those space-charge potentials in the following long-term
331 simulation. This method significantly reduces the computing time and yields

332 qualitatively reasonable simulation results in comparison to the self-consistent
333 space-charge simulation in the examples used in this study. The frozen space-
334 charge model can be used when the beam charge density does not vary signif-
335 icantly from turn to turn. This corresponds to the situation that the particle
336 beam is not subject to any coherent instability or strong resonance.

337 6. ACKNOWLEDGEMENTS

338 We would like to thank discussion with Dr. C. Mitchell. This work was
339 supported by the U.S. Department of Energy under Contract No. DE-AC02-
340 05CH11231 and used computer resources at the National Energy Research Sci-
341 entific Computing Center.

342 References

- 343 [1] A. Friedman, D. P. Grote, and I. Haber, *Phys. Fluids B* 4 , 2203 (1992).
- 344 [2] H. Takeda and J. H. Billen, Recent developments of the accelerator design
345 code PARMILA, in *Proc. XIX International Linac Conference, Chicago,*
346 *August 1998, p. 156.*
- 347 [3] S. Machida and M. Ikegami, in *AIP Conf. Proc* 448, p.73 (1998).
- 348 [4] F. W. Jones and H. O. Schoenauer, *Proc of PAC1999*, p. 2933, 1999.
- 349 [5] J. Qiang, R. D. Ryne, S. Habib, V. Decyk, *J. Comput. Phys.* **163**, 434,
350 2000.
- 351 [6] P. N. Ostroumov and K. W. Shepard. *Phys. Rev. ST. Accel. Beams* 11,
352 030101 (2001).
- 353 [7] R. Duperrier, *Phys. Rev. ST Accel. Beams* **3**, 124201, 2000.

- 354 [8] J. D. Galambos, S. Danilov, D. Jeon, J. A. Holmes, and D. K. Olsen, F.
355 Neri and M. Plum, Phys. Rev. ST Accel. Beams **3**, 034201, (2000).
- 356 [9] H. Qin, R. C. Davidson, W. W. Lee, and R. Kolesnikov, Nucl. Instr. Meth.
357 in Phys. Res. A 464, 477 (2001).
- 358 [10] G. Franchetti, I. Hofmann, M. Giovannozzi, M. Martini, and E. Metral,
359 Phys. Rev. ST Accel. Beams **6**, 124201, (2003).
- 360 [11] J. Qiang, S. Lidia, R. D. Ryne, and C. Limborg-Deprey, Phys. Rev. ST
361 Accel. Beams **9**, 044204, 2006.
- 362 [12] J. Amundson, P. Spentzouris, J. Qiang and R. Ryne, J. Comp. Phys. vol.
363 211, 229 (2006).
- 364 [13] J. Qiang, R. D. Ryne, M. Venturini, A. A. Zholents, I. V. Pogorelov, Phys.
365 Rev. ST Accel. Beams, 12, 100702 (2009).
- 366 [14] http://amas.web.psi.ch/docs/opal/opal_user_guide.pdf.
- 367 [15] P. J. Channell and C. Scovel, Nonlinearity **3**, p.231 (1990).
- 368 [16] T. J. Stuchi, Brazilian J. Phys. **32**, p. 958 (2002).
- 369 [17] J. Qiang, Phys. Rev. Accel. Beams **20**, 014203, (2017).
- 370 [18] J. Qiang, Phys. Rev. Accel. Beams **21**, 054201, (2018).
- 371 [19] H. Okuda and C. K. Birdsall, Phys. Fluids 13, p. 2123, (1970).
- 372 [20] J. Struckmeier, Phys. Rev. ST Accel. Beams 3, 034202 (2000).
- 373 [21] I. Hofmann and O. Boine-Frankenheim, Phys. Rev. ST Accel. Beams 17,
374 124201 (2014).
- 375 [22] O. Boine-Frankenheim, I. Hofmann, J. Struckmeier, and S. Appel, Nucl.
376 Instrum. Methods Phys. Res., Sect. A 770, 164 (2015).

- 377 [23] F. Kesting and G. Franchetti, Phys. Rev. ST Accel. Beams 18, 114201
378 (2015).
- 379 [24] R.W. Hockney, J.W. Eastwood, Computer Simulation Using Particles,
380 Adam Hilger, New York, 1988.
- 381 [25] C. K. Birdsall and A. B. Langdon, Plasma Physics Via Computer Simula-
382 tion, Taylor and Francis, New York, 2005.
- 383 [26] <http://mad.web.cern.ch/mad/>.
- 384 [27] R. D. Ryne, “Computational Methods in Accelerator Physics,” US Particle
385 Accelerator class note, 2012.
- 386 [28] A. J. Dragt, “Lie Methods for Nonlinear Dynamics with Applications to
387 Accelerator Physics,” 2016.
- 388 [29] A. B. Langdon, J. Comp. Phys 12, p. 247 (1973).
- 389 [30] S. Machida, in Proc. of IPAC2015, Richmond, VA, USA, p. 2402, 2015.
- 390 [31] H. Bartosik et al., in Proc. of HB2014, East-Lansing, MI, USA, p. 249,
391 2014.
- 392 [32] G. Franchetti, S. Gilardoni, A. Huschauer, F. Schmidt, and R. Wasef, Phys.
393 Rev. Accel. Beams 20, 081006 (2017).